

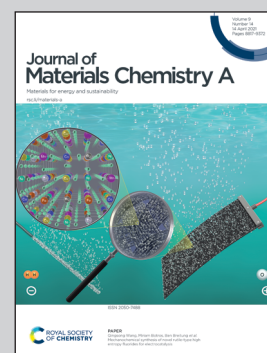


Highlighting a study about Hybrid Nanostructure Derived from a Metal–Organic Framework for Photocatalytic Synthesis by Mohammad Yusuf from IOM group under Prof. Kang Hyun Park, Pusan National University.

Core-shell $\text{Cu}_2\text{S}:\text{NiS}_2@\text{C}$ hybrid nanostructure derived from a metal-organic framework with graphene oxide for photocatalytic synthesis of N-substituted derivatives

A Cu:Ni metal-organic framework (MOF) modified with graphene oxide (GO) was fabricated by a facile and convenient process. Subsequently, the Cu:Ni sulfide encapsulated on porous C with reduced GO ($\text{Cu}_2\text{S}:\text{NiS}_2@\text{C}/\text{rGO}$) as a core-shell nanostructure was achieved using a MOF (Cu:Ni-BTEC/GO). The $\text{Cu}_2\text{S}:\text{NiS}_2@\text{C}/\text{rGO}$ with hybrid structure showed superior photocatalytic activity for producing N-substituted derivatives through three kinds of oxidative coupling reactions. Moreover, the MOF-derived photocatalyst exhibited good reusability and stability.

As featured in:



See Kang Hyun Park *et al.*,
J. Mater. Chem. A, 2021, **9**, 9018.

Cite this: *J. Mater. Chem. A*, 2021, 9, 9018

Core–shell Cu₂S:NiS₂@C hybrid nanostructure derived from a metal–organic framework with graphene oxide for photocatalytic synthesis of N-substituted derivatives†

Mohammad Yusuf,^a Shamim Ahmed Hira,^a Hyeonhan Lim,^a Sehwan Song,^b Sungkyun Park^b and Kang Hyun Park^{ib}*^a

Recently, photocatalysis has attracted considerable interest, leading to opportunities for using renewable energy sources. A Cu:Ni metal–organic framework (MOF) modified with graphene oxide (GO) was fabricated by a facile and convenient process. Subsequently, the Cu:Ni sulfide encapsulated on porous C with reduced GO (Cu₂S:NiS₂@C/rGO) as a core–shell nanostructure was achieved using a MOF (Cu:Ni-BTEC/GO). Cu₂S:NiS₂@C/rGO with a hybrid structure showed superior photocatalytic activity for producing N-substituted derivatives through three kinds of oxidative coupling reactions. Moreover, the MOF-derived photocatalyst exhibited good reusability and stability. The excellent photocatalytic behavior of MOF-derived bimetallic chalcogenides would channel further interest in the design, synthesis, and modification of MOFs as photocatalysts for diverse applications.

Received 7th January 2021
Accepted 22nd February 2021

DOI: 10.1039/d1ta00159k

rsc.li/materials-a

Introduction

Multifunctional hybrid catalysts contain metallic nanoparticles, and the support represents an effective strategy for wide-ranging applications, especially in organic and photochemical reactions. Numerous hybrid catalysts, particularly core–shell, yolk–shell, double-shell, hollow, and their relative structures, have been developed and utilized for energy storage, sensing, water treatment, catalysis, and biomedical applications.^{1,2} However, well-defined structures with effective methods and excellent catalytic performance are still being studied.

Recently, synthesizing various hybrid nanostructures from metal–organic frameworks (MOFs) has generated considerable interest for diverse applications, especially in catalysis.^{3,4} Nevertheless, MOF-based multifunctional nanostructures still have some limitations, which generally restrict their applications.⁵ Therefore, tailoring MOFs with other functional materials, such as polymers, semiconductors, and graphene oxide (GO), can be an excellent alternative to overcome the limited abilities of single MOFs.^{6–9} Following recent studies, incorporating MOFs and graphene-based materials can integrate the benefits of the individual components owing to their improved stability, modified structure, enlarged surface area, diminished

aggregation, enhanced dispersion, and increased catalytic activity.¹⁰ Furthermore, inorganic metals can be used as precursors of metals or metal oxides, and the organic linker can act as a template for establishing a nanoporous carbon support. Hence, a MOF-based multifunctional structure can be obtained by deriving the component of the MOF. MOF-based derivatives overcome the limitations of the raw stability of MOFs at high temperatures and harsh chemical environments.^{4,5,11}

MOF derivatives are usually achieved through chemical reduction and thermal treatment or a combination of both methods. In addition, thermal treatment (direct pyrolysis), including carbonization, phosphorization, and sulfurization, is an effective and easy method. Direct pyrolysis by sulfurization can transform the structure into an S-doped multifunctional structure consisting of a metal and porous carbon. Furthermore, this method is a promising strategy for fabricating metal-sulfide-based multifunctional structures.^{4,12–14} Metal sulfides (chalcogenides) have gained research attention for fuel cells, environmental remediation, and photocatalysis owing to many materials with readily controllable mechanical, optical, physical, and chemical properties. Metal sulfides have various structures that can be enriched by adding different metal ions and templates; moreover, these sulfides have an appropriate band gap that can be controlled through the composition. This ability is suitable for developing photocatalysts using metal-sulfide-based materials.^{15,16} In addition, the development of photocatalysts based on the multistructural design of metal chalcogenides, especially for organic reactions, remains a challenge. Among the numerous structural engineering options,

^aDepartment of Chemistry and Chemistry Institute for Functional Materials, Pusan National University, Busan, 46241, Republic of Korea. E-mail: chemistry@pusan.ac.kr

^bDepartment of Physics, Pusan National University, Busan, 46241, Republic of Korea

† Electronic supplementary information (ESI) available. See DOI: 10.1039/d1ta00159k

semiconductor TiO₂ with refined core-shell and arranged structural designs provides an example of the advantages of structural modification and multicomponent architecture owing to critical developments including photostability, charge-carrier separation, light absorption, and surface properties.¹⁷ Therefore, the opportunities for the structural development of metal sulfides utilized for highly effective photocatalysis are remarkably abundant based on this concept.

Moreover, metal-metal oxide catalysts with a Cu- or Ni-based multistructural design have been consistently utilized for organic transformations to reduce or replace noble metals and to enlarge hybrid material catalysts.^{18–24} In addition, multicomponent engineered metal hybrid nanocatalysts have been developed to achieve highly active catalysts with excellent stability.^{1,18} However, intense temperature and pressure levels remain a risk that must be addressed. Light-harvesting materials for photocatalyst systems can overcome this limitation to achieve mild conditions and open opportunities for using renewable energy sources.^{25,26}

In contrast, N-containing organic compounds are indispensable components in modern synthetic organic chemistry. Among these compounds, N-heterocyclic and N-aryl species are promising biologically active compounds, pharmaceuticals, and fine chemicals with tremendous applications from laboratory- to industrial-scale production.^{27–31} Various approaches for updating N-heterocyclic and N-aryl derivatives have been implemented with convenient and validated synthetic routes. One promising technique is the oxidative coupling reaction.^{32–37} However, the search for an efficient method and catalyst system for oxidative coupling reactions is ongoing.

Based on the above considerations, developing a multifunctional core-shell nanostructure from a MOF derivative containing non-noble metals (Cu and Ni) and tailored with GO could be a promising strategy for oxidative coupling reactions forming C–N bonds. A hybrid nanostructure of Cu and Ni chalcogenides was fabricated from a MOF derivative through a simple method. In addition, the structures of Cu₂S:NiS₂@C/rGO increased the photocatalytic activity for the synthesis of N-substituted derivatives.

Experimental

Materials and instrumentation

All chemicals were purchased from Sigma-Aldrich, TCI, Acros, Alfa-Aesar, or Daejung Company and were used as obtained without purification. The properties of the catalysts were analyzed *via* X-ray diffraction (XRD) using a diffractometer (X'Pert³ MRD, Malvern Panalytical Ltd.). The morphologies of the catalysts were characterized *via* field emission scanning electron microscopy (SEM) using a microscope (SUPRA 40VP, Carl ZEISS) and transmission electron microscopy (TEM) using a high-resolution microscope (TALOS F200X, FEI) at 200 keV with integrated energy dispersive X-ray (EDX) mapping. Surface chemical state data were obtained *via* X-ray photoelectron spectroscopy (XPS) using a spectrometer (AXIS Supra, Kratos Analytical Ltd.). The elemental composition was determined *via* inductively coupled plasma optical emission spectroscopy (ICP-

OES) using an optical system (Optima 8300, PerkinElmer Inc.). The properties of the surface structure were identified using N₂ sorption isotherms using a Brunauer–Emmett–Teller (BET) surface area analyzer (ASAP 2020, Micromeritics Instrument Corp.). Additional characterization was performed *via* UV-Vis diffuse reflectance spectroscopy (DRS) using a UV-Vis/near infrared spectrophotometer (V-770, JASCO Corp.) and a micro-Raman spectrometer (FEX, NOST), respectively. Subsequently, the photocatalyst was identified using a gas chromatography–mass spectrometry (GC-MS) system (QP2010 SE, Shimadzu Corp.).

Materials synthesis

Synthesis of Cu:Ni-BTEC/GO. A GO suspension was prepared by continuously dispersing GO powder (50 mg) in deionized water *via* ultrasonication at an amplitude of 30% for 30 min. Approximately 1.25 mmol of both Cu(NO₃)₂·2.5H₂O and Ni(NO₃)₂·6H₂O was then dissolved in 25 mL of dimethylformamide (DMF). Subsequently, 1.25 mmol of 1,2,4,5-benzenetetracarboxylic acid (H₄BTEC) was added to the solution. The reaction system was combined with the GO suspension, transferred to a Teflon-lined autoclave (100 mL), and the nanoparticles were continuously grown at 150 °C for 3 h. The reaction was then naturally cooled at room temperature. Finally, the prepared catalyst was collected, rinsed with DMF and methanol (MeOH), and subsequently dried. Cu-BTEC/GO, Ni-BTEC/GO, and Cu:Ni-BTEC were synthesized using the same analog process for comparison.

Synthesis of Cu₂S:NiS₂@C/rGO. The as-prepared Cu:Ni-BTEC/GO and S powder in a 1 : 2 ratio were placed in two separate alumina crucible boats in a tube furnace. The S powder was fixed upstream following the sample at a distance of ±10 cm. The samples were annealed stepwise in a flowing N₂ atmosphere at 250 °C for 1 h and then continuously at 350 °C for 1 h at a heating rate of 2 °C min^{−1}. The product was collected for further analyses.

Photocatalytic activity

Chan–Lam coupling reactions of phenylboronic acid and imidazole. A mixture of phenylboronic acid (0.5 mmol), imidazole (0.5 mmol), catalyst (5 mg), and solvent (4 mL; MeOH-to-H₂O ratio was 3 : 1) was placed in a 25 mL quartz round-bottom flask and stirred at room temperature (25 °C). After the reaction was completed, MeOH (5 mL) was added, and the catalyst was separated by centrifugation. Subsequently, the product was extracted with CH₂Cl₂, dehydrated with MgSO₄, and concentrated using a rotary evaporator.

Cyclization of o-phenylenediamine and aldehyde. In a 25 mL quartz round-bottom flask with a magnetic stirrer, 1,2-phenylenediamine (0.25 mmol), aromatic aldehyde (0.25 mmol), ethanol (EtOH) (3 mL), and catalyst (2.5 mg) were added. After the reaction was completed, EtOH (5 mL) was added. Subsequently, the catalyst was separated, extracted with ethyl acetate, dehydrated, and concentrated to obtain the desired product.

Oxidative homocoupling of benzylamine. Benzylamine (0.25 mmol), catalyst (2.5 mg), and acetonitrile (CH₃CN, 3 mL) were

placed in a quartz round-bottom flask. After the reaction was completed, CH_3CN (5 mL) was added. Subsequently, the catalyst was separated and concentrated using a rotary evaporator.

All the reactions were conducted under irradiation from a xenon arc lamp 300 W (Newport Corp.) with a cut-off of 400–800 nm and an intensity of 200 mW cm^{-2} . The lamp was equipped with specific longpass filters (cut-on of 400, 455, 515, and 610 nm) to suppress the transmission at selected frequencies (for example, a cut-on of 400 nm blocks <400 wavelengths), a liquid filter to minimize heat and remove IR wavelengths (>900 nm), an IR cut-off to obstruct >800 nm wavelengths, and an Air Mass 1.5G filter to match AM1.5g natural solar conditions (solar spectrum). The reaction was monitoring by thin layer chromatography. Subsequently, product conversion was measured *via* GC-MS.

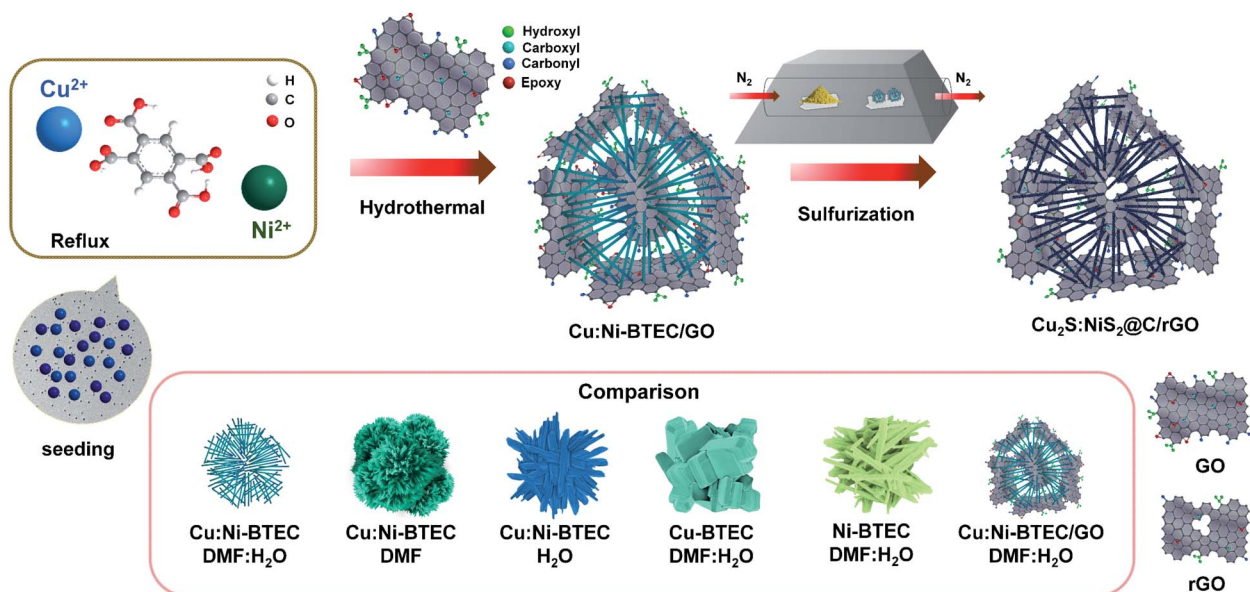
Results and discussion

The synthesized bimetallic (Cu and Ni) sulfide with a multi-functional structure was obtained by simple derivation of a MOF. The synthetic strategy for Cu:Ni-MOF/GO and its derivative $\text{Cu}_2\text{S:NiS}_2@\text{C/rGO}$ is illustrated in Scheme 1. First, a novel bimetallic GO-modified Cu:Ni-MOF was fabricated through a hydrothermal method. The new ligand for this bimetallic MOF was applied using H_4BTEC , which is rich in carboxylate groups incorporated with the metal center and O-containing functional groups from GO (epoxy, hydroxyl, and carboxyl). The seeding of the MOF was first achieved under reflux conditions, confirmed by TEM (Fig. S1, ESI[†]). The continuous mixing with GO by the hydrothermal method formed a Cu:Ni-MOF/GO structure. Subsequently, the transformation of the MOF composite into metal sulfide was achieved through *in situ* carbonization and sulfurization with S powder under inert (N_2) conditions. The remarkable structure

of the bimetallic sulfide trapped in the C matrix tailored with rGO ($\text{Cu}_2\text{S:NiS}_2@\text{C/rGO}$) was obtained by *in situ* growth of nanoparticles derived from H_4BTEC ligands and GO from direct carbonization and sulfurization.

The morphologies of the MOF and its derivative were identified *via* SEM and TEM. The nanorod form of the Cu:Ni-BTEC MOF was observed using a solvent consisting of DMF and water (H_2O) in a 1 : 1 volume ratio (Fig. 1a). The MOF exhibited a size distribution of approximately 32 nm (Fig. S2[†]). However, a flower-like structure was obtained when only DMF was used as the solvent (Fig. 1c). Moreover, H_2O has a high affinity for coordinating with the metal centers compared to DMF; hence, the cage grew big when only H_2O was used as the solvent, as confirmed by a micro urchin-like shape (Fig. 1e). For comparison, the metals Cu and Ni were identified as well (Fig. 1g and i). The Cu-MOF and Ni-MOF grew toward the tetragonal plate and hexagonal rod, respectively.³⁸

Moreover, GO was used to modify the structure and enhance the stability, photo-properties, and catalytic activity.^{10,39} The GO-modified MOF was identified by the GO layer, as shown in Fig. 1b, 2a, b and 3(i). For comparison, the morphologies of Cu:Ni-BTEC/GO (with H_2O or DMF as the solvent), Cu-BTEC/GO, and Ni-BTEC/GO are presented in Fig. 1 (right side). After heat treatment, the MOF transformed into Cu and Ni sulfide embedded in the C matrix of the rGO layer ($\text{Cu}_2\text{S:NiS}_2@\text{C/rGO}$). The rod shape was maintained; however, the surface changed from smooth to rough. Fig. 3 shows the additional morphological details; such details were evaluated *via* TEM with integrated EDX mapping. Cu and Ni sulfide nanoparticles were incorporated into the C shell with a size of approximately 10 nm. Furthermore, the porous C shell and the graphene layer were clearly confirmed by high-angle annular dark-field (HAADF), as shown in Fig. 3(ii)c. The presence of Cu, Ni, S, and C was confirmed from the elemental mapping (Fig. 3(i–ii)d–



Scheme 1 Schematic illustration of Cu:Ni-BTEC/GO and $\text{Cu}_2\text{S:NiS}_2@\text{C/rGO}$.

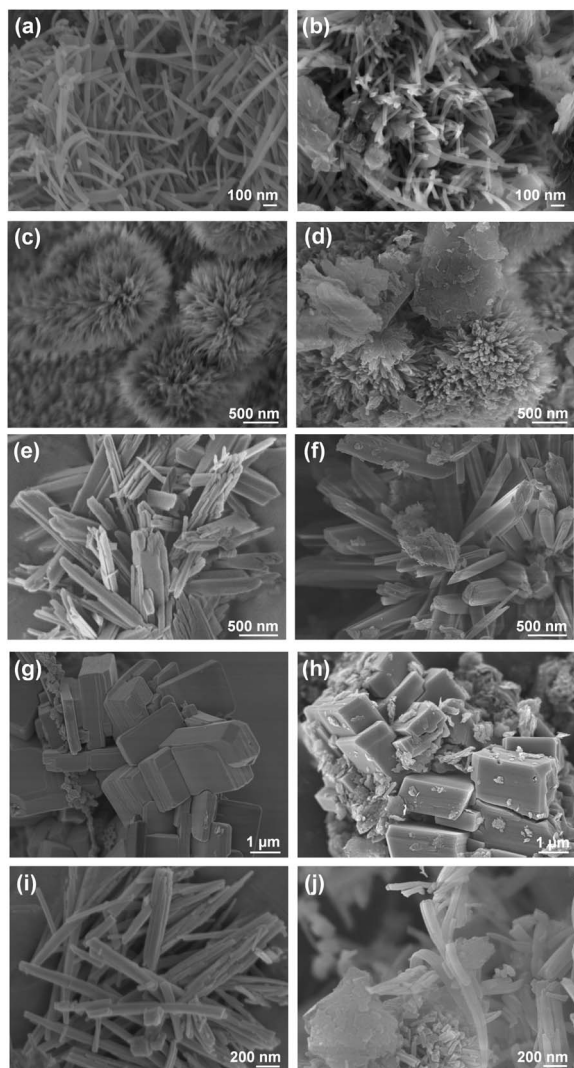


Fig. 1 SEM images of (a) Cu:Ni-BTEC (b) Cu:Ni-BTEC/GO in DMF:H₂O, (c) Cu:Ni-BTEC (d) Cu:Ni-BTEC/GO in DMF, (e) Cu:Ni-BTEC (f) Cu:Ni-BTEC/GO in H₂O, (g) Cu-BTEC (h) Cu-BTEC/GO in DMF:H₂O, and (i) Ni-BTEC (j) Ni-BTEC/GO in DMF:H₂O.

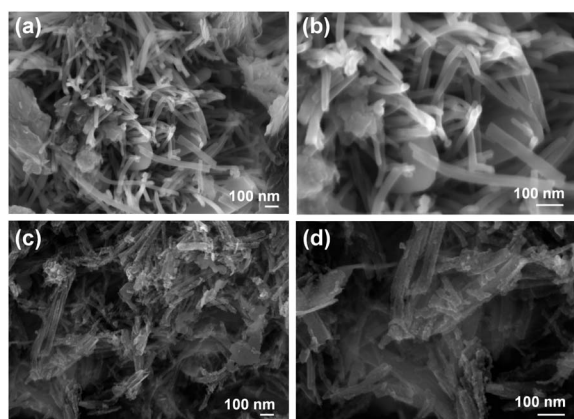


Fig. 2 SEM image of (a and b) Cu:Ni-BTEC/GO and (c and d) Cu₂S:NiS₂@C/rGO.

h). In addition, the Cu, Ni, and S contents (wt%) in the catalyst before and after calcination were confirmed by ICP-OES (Table S1†). Here, a hybrid core-shell nanostructure of a bimetallic (Cu and Ni) sulfide encapsulated on porous C and modified with GO was successfully formed from an MOF derivative.

The XRD patterns in Fig. 4a indicate that the bimetallic sulfide was obtained after the calcination of Cu:Ni-BTEC/GO. For comparison, the other MOFs and MOFs without GO loading are shown in Fig. S3†. The peaks at 26.67°, 30.00°, 46.65°, and 54.99° for Cu₂S and 27.26°, 31.59°, 35.46°, 38.94°, 45.24°, 53.43°, 56.00°, 58.79°, and 60.95° for NiS₂ were attributed to the hexagonal Cu₂S (ICSD#020560) and triclinic NiS₂ (ICSD#022369), respectively. The broad peak at around 15–25° indicated the C and rGO peaks. Moreover, the successful synthesis of bimetallic sulfide (Cu₂S:NiS₂@C/rGO) was confirmed by the Fourier transform (FT) patterns from the high-resolution TEM images, as shown in Fig. 4b–d. The interplanar distances were approximately 0.28 and 0.32 nm, which were in agreement with the (200) lattice point of the NiS₂ and the (002) lattice point of Cu₂S structures, respectively.

The chemical surface and composition states were analyzed *via* XPS, and the results are shown in Fig. 5. Cu, Ni, S, O, and C appeared in the survey scan spectra of the samples (Fig. S4†). The C–C binding energy (BE; 284.5 eV) was used for calibration to further deconvolute the spectra. As shown in Fig. 5a, the Cu 2p peak at a BE of 934.96 eV was assigned to the Cu–O bond of Cu-BTEC, and this peak was validated with the Cu²⁺ satellite peak. The shift of Cu 2p_{3/2} to the lower energy (932.29 eV) and the disappearance of the satellite peak confirmed the successful sulfurization process, which produced the Cu₂S structure. The deconvolution of Ni 2p (Fig. 5b) for the derived MOF at BEs of 853.73 and 855.53 eV demonstrated a BE that was considerably lower than that of the underived MOF. This result confirms that Ni-BTEC peaks were transformed into those of the NiS₂ structure and impurities (Ni(OH)₂). In addition, as shown in Fig. 5c, the S 2p at BEs from 160 eV to 168 eV was attributed to the presence of Cu–S and Ni–S 2p_{3/2} (2p_{1/2}) at a BE of 162.25 (163.43) eV, C–S 2p_{3/2} (2p_{1/2}) at a BE of 163.70 (164.88) eV, and impurities (SO₃²⁻) at a BE of 167.00 eV. The C 1s deconvolution spectrum exhibited the features of C=O–OH, C–O–C, C=C (sp²), and C–C/C–H (sp³) for Cu:Ni-BTEC/GO, indicating the characteristic of C from the BTEC ligand and GO (Fig. 5d). After the calcination process, the decreased number of carboxyl and epoxy functional groups and the increased C=C (sp²) and C–C/C–H (sp³) of Cu₂S:NiS₂@C/rGO were attributed to the transformation of the ligand and GO into the C matrix and rGO structure, respectively.⁴⁰

In addition, Raman spectroscopic analyses were performed to examine and classify the structural and electronic conjugation states of GO after thermal treatment. The two specific features of the G band (1575 cm⁻¹) and D band (1350 cm⁻¹) were obtained, and these features were assigned to the E_{2g} symmetry of sp² C atoms and the breathing mode of A_{1g} symmetry, respectively (Fig. 6a). The intensity ratio of the D to the G band (*I_D/I_G*) for Cu₂S:NiS₂@C/rGO (0.70) was higher than that of Cu:Ni-BTEC/GO (0.46), implying that the thermal process enhanced the reduction and generated defects in the

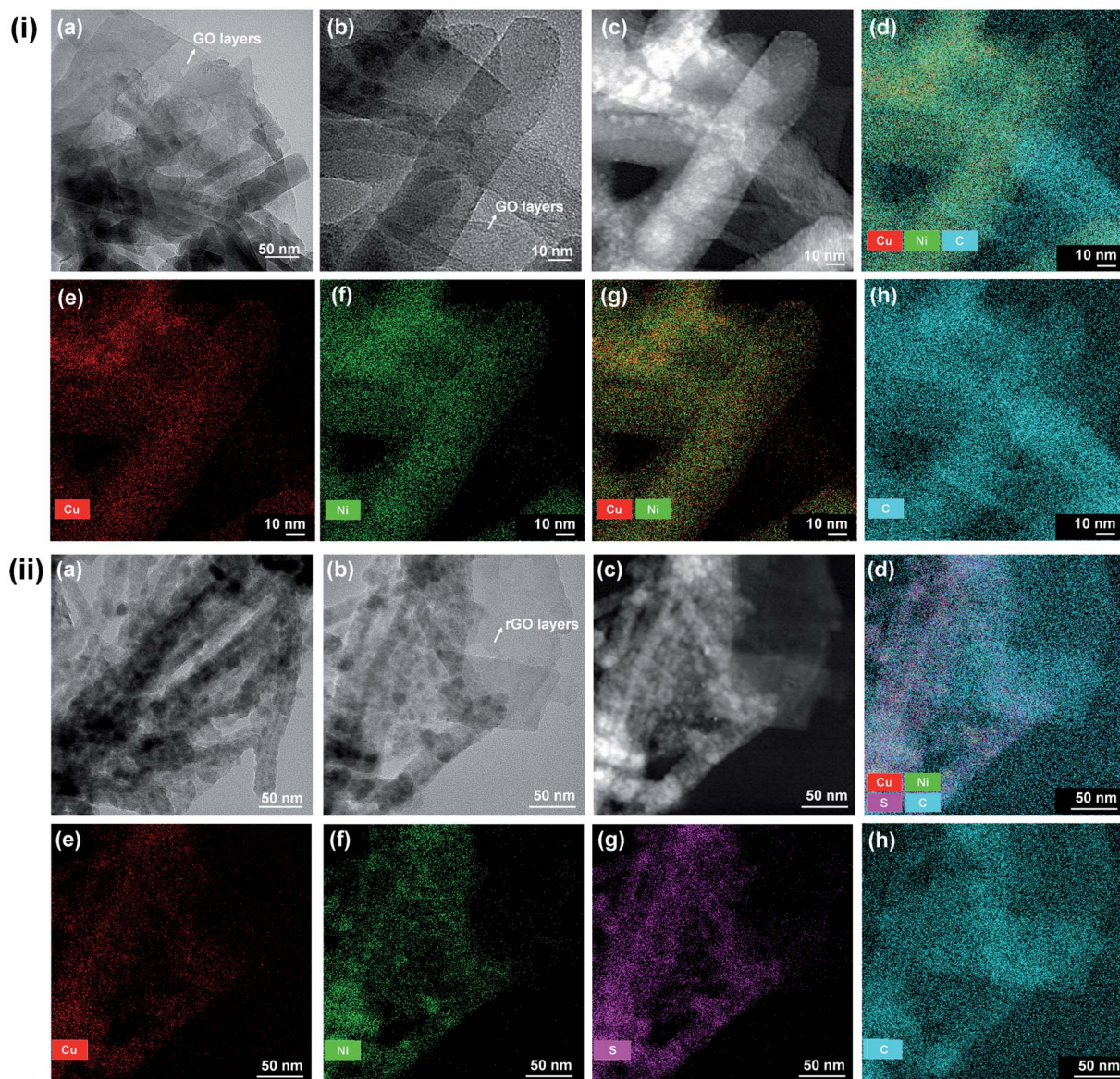


Fig. 3 TEM image of (i) Cu:Ni-BTEC/GO and (ii) $\text{Cu}_2\text{S}:\text{NiS}_2@\text{C}/\text{rGO}$.

GO structure.⁴¹ To further verify the features of the surface structures of the as-prepared catalysts, N_2 sorption isotherms were obtained, as shown in Fig. 6b. All the catalysts displayed

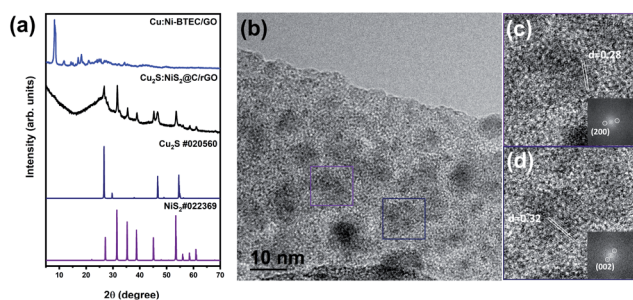


Fig. 4 (a) XRD patterns of Cu:Ni-BTEC/GO and $\text{Cu}_2\text{S}:\text{NiS}_2@\text{C}/\text{rGO}$, (b and c) high-resolution TEM image of $\text{Cu}_2\text{S}:\text{NiS}_2@\text{C}/\text{rGO}$, inset: FT patterns of Cu_2S and NiS_2 .

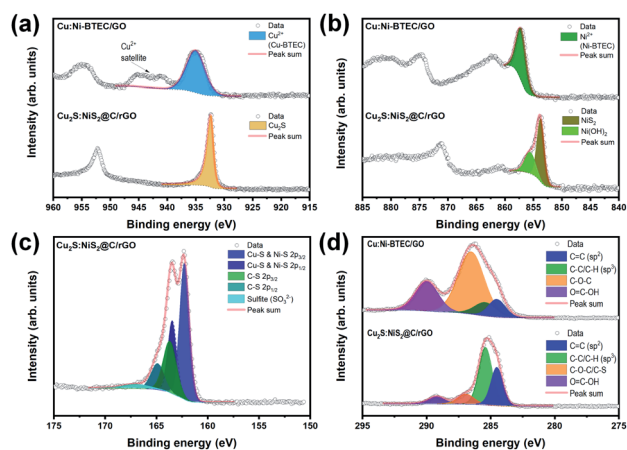


Fig. 5 (a) XPS spectra of Cu:Ni-BTEC/GO and $\text{Cu}_2\text{S}:\text{NiS}_2@\text{C}/\text{rGO}$ (a) Cu 2p lines, (b) Ni 2p lines, (c) S 2p lines and (d) C 1s lines.

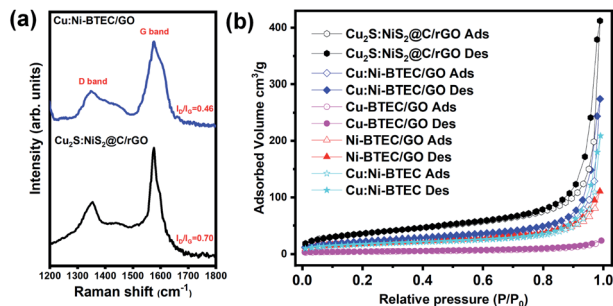


Fig. 6 (a) Raman spectra of Cu:Ni-BTEC/GO and $\text{Cu}_2\text{S}:\text{NiS}_2@\text{C}/\text{rGO}$, (b) N_2 sorption isotherms of various Cu:Ni-BTEC/GO and its derivatives.

a characteristic type IV isotherm and were close to hysteresis type H3. The BET surface area of $\text{Cu}_2\text{S}:\text{NiS}_2@\text{C}/\text{rGO}$ was larger than that of Cu:Ni-BTEC/GO. The calcination process increased the BET surface area of the Cu:Ni-MOF due to the exposure of more surface-active sites as far as possible up to

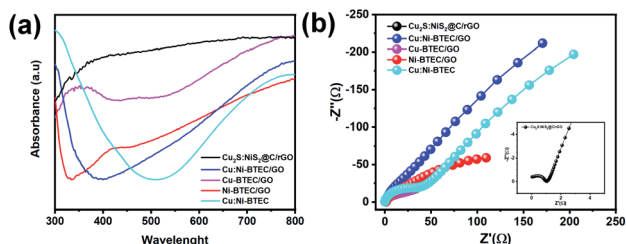


Fig. 7 (a) UV-Vis DRS spectroscopy and (b) EIS spectra of various Cu:Ni-BTEC/GO and its derivatives.

aggregation of the active NPs.⁸ For comparison, the BET surface area, pore volume, and average pore size of the other prepared materials are displayed in Table S2.† Using the Barrett–Joyner–Halenda method, the average pore size distribution was calculated for all the materials assigned to the mesoporous material.⁴²

UV-Vis DRS was used to identify the spectral characteristics of the as-synthesized catalysts, as shown in Fig. 7a. The as-prepared catalysts before the sulfurization process showed UV adsorption in the <400 nm region and increased adsorption in the visible region at >500 nm. However, after sulfurization, the adsorption expanded from the UV to the visible area for $\text{Cu}_2\text{S}:\text{NiS}_2@\text{C}/\text{rGO}$, highlighting its superior optical properties compared to other catalysts. The photogenerated charge transfer properties were then evaluated through electrochemical impedance spectroscopy (EIS) (Fig. 7b). Compared to the other materials, $\text{Cu}_2\text{S}:\text{NiS}_2@\text{C}/\text{rGO}$ exhibited small semi-circles, indicating low charge transfer resistance. This result was related to large charge separation efficiency, resulting in remarkably decreased photorecombination of electron-hole pairs.

The photocatalytic efficiencies of the synthesized materials were initially utilized for C–N bonds *via* the Chan–Lam coupling reaction using the coupling of arylboronic acid and imidazole as a model reaction. Table 1 shows the various conditions for optimization. A conversion of >97% was achieved through $\text{Cu}_2\text{S}:\text{NiS}_2@\text{C}/\text{rGO}$ in entry 4. The photocatalytic activities of the materials followed the order $\text{Cu}_2\text{S}:\text{NiS}_2@\text{C}/\text{rGO} > \text{Cu}:\text{Ni-BTEC}/\text{GO} > \text{Cu-BTEC}/\text{GO} > \text{Ni-BTEC}/\text{GO}$ (N. R.) = Cu:Ni-BTEC (N. R.) (entries 4–11). The combination of GO and Cu:Ni-MOF provided a synergetic effect for better reaction, as indicated by entries 8 (Cu:Ni-BTEC/GO) and 9 (Cu:Ni-BTEC).

Table 1 The photocatalytic activity of $\text{Cu}_2\text{S}:\text{NiS}_2@\text{C}/\text{rGO}$ and its derivatives for C–N coupling of phenylboronic acid and imidazole^a

Entry	Catalyst	Solvent	Time (h)	Conv. ^b (%)	Selec. ^b (%)
1	$\text{Cu}_2\text{S}:\text{NiS}_2@\text{C}/\text{rGO}$	MeOH	3 h	76	60
2	$\text{Cu}_2\text{S}:\text{NiS}_2@\text{C}/\text{rGO}$	MeOH	6 h	88	98
3	$\text{Cu}_2\text{S}:\text{NiS}_2@\text{C}/\text{rGO}$	MeOH : H ₂ O (1 : 1)	6 h	94	80
4	$\text{Cu}_2\text{S}:\text{NiS}_2@\text{C}/\text{rGO}$	MeOH : H ₂ O (3 : 1)	6 h	97	94
5	$\text{Cu}_2\text{S}:\text{NiS}_2@\text{C}/\text{rGO}$	H ₂ O	6 h	N.R	—
6	$\text{Cu}_2\text{S}:\text{NiS}_2@\text{C}/\text{rGO}$	EtOH : H ₂ O (3 : 1)	6 h	74	94
7	$\text{Cu}_2\text{S}:\text{NiS}_2@\text{C}/\text{rGO}$	CH ₃ CN : H ₂ O (3 : 1)	6 h	99	94
8	Cu:Ni-BTEC/GO	MeOH : H ₂ O (3 : 1)	6 h	24	94
9	Cu:Ni-BTEC	MeOH : H ₂ O (3 : 1)	6 h	N.R	—
10	Cu-BTEC/GO (S ^c)	MeOH : H ₂ O (3 : 1)	6 h	15 (72)	94 (94)
11	Ni-BTEC/GO (S ^c)	MeOH : H ₂ O (3 : 1)	6 h	N.R (15)	— (90)
12 ^d	GO, GO AHT, GO ACT	MeOH : H ₂ O (3 : 1)	6 h	N.R	—

^a Reaction conditions: 0.5 mmol of **1a** and **1b**, 4 mL solvent, 5 mg of photocatalyst $\text{Cu}_2\text{S}:\text{NiS}_2@\text{C}/\text{rGO}$, 10 mg of entry 8–12. The reactions were conducted in air at room temperature (r.t) under Xe-lamp irradiation (400–800 nm) with a light intensity of 200 mW cm⁻². ^b Conversions and selectivity determined by GC-MS analysis. ^c Sulfurization of Cu and Ni-MOF. ^d AHT is after hydrothermal (reaction) treatment, ACT is after calcination treatment.

The Cu-MOF after sulfurization process tends to be more active compared to the sulfurized Ni-MOF (entry 10–11). Cu and Ni are widely used for C–N coupling reactions as an alternative to noble metal Pd. However, few studies were conducted using Ni or Cu:Ni catalysts relative to Cu catalysis.^{33,43} The bimetallic system of Cu:Ni displayed better photocatalytic efficiency compared to the single Cu or Ni attributed to the synergetic effect. In addition, by introducing a bimetallic MOF, the downsizing of single Cu and Ni micro-MOF was developed to produce a Cu:Ni nano-MOF (Fig. 1), which improves the catalytic selectivity and activity. This result provides an encouraging approach to the further synthesis of nano-MOFs, as a nano-MOF is still a challenge.^{44,45} For comparison, the bare GO after hydrothermal and calcination treatment was identified (entry 12) and no conversion was observed. Moreover, the solvent played a major role in the photocatalytic reaction. Excellent conversion was achieved using a 3 : 1 mixture of the protic solvent (MeOH) and H₂O. Decreasing the polarity of the solvent to EtOH reduced the conversion, whereas increasing the polarity of the aprotic solvent CH₃CN enhanced the conversion (entry 3–7). However, MeOH is an environmentally preferable solvent to CH₃CN;⁴⁶ hence, this condition was used in the next step. Furthermore, another solvent condition was determined for crosschecking (entry 1–7). A comparative study with a previously reported catalyst for C–N coupling is shown in the ESI (Table S3†). The high conversion achieved by the free base, free additional oxidation agent, and green solvent provided a convenient operational protocol and minimized the environmental issues for the C–N oxidative coupling reaction.

The effect of light on the enhanced catalytic activity was explored in terms of intensity and wavelength dependency. First, as shown in Fig. 8a, the intensity was varied from 100 mW cm⁻² to 200 mW cm⁻² with 20 intervals. The conversion at 100 mW cm⁻² (75%) was better than that under dark conditions (29%). Furthermore, increasing the intensity improved the conversion of substrates; the optimum conversion was when

irradiated at 200 mW cm⁻². Second, to confirm the effect of the irradiation wavelength, various longpass filters (cut-on) were applied to remove transmission below a specific wavelength (Fig. 8b). Filters of 400, 455, 515, and 610 nm were used, and the conversions at 400–800, 455–800, 515–800, and 610–800 nm wavelengths were 97%, 86%, 72%, and 52%, respectively. By dividing the conversion under the light and dark conditions (25%) as calculation [(97–86)/(97–29) × 100%], the overall light-induced conversion under specific wavelengths of 400–455, 455–515, 515–610, and 610–800 nm was obtained to be 16%, 21%, 29%, and 34%, respectively. These data were consistent with the UV-Vis DRS absorption of Cu₂S:NiS₂@C/rGO, as shown in Fig. 8c. Therefore, the light-driven capacity of Cu₂S:NiS₂@C/rGO through the synergetic effect of the composition and multifunctional structure considerably influenced the photocatalytic activity for the N-arylation of imidazole with arylboronic acid.

Photocatalysis was substantially related to the electron–hole transfer of the material *via* light irradiation. Therefore, the effects of the electron and hole scavengers were investigated (Fig. 8d).⁴⁷ Carbon tetrachloride (CCl₄) is an electron quencher for capturing the electrons of Cu₂S:NiS₂@C/rGO. With the addition of CCl₄, no desired C–N coupling product was achieved. Moreover, the addition of the hole quencher triethanolamine (TEA) resulted in considerably decreased conversion. This phenomenon indicates that the photo-hole production was successfully blocked. The suggested reaction mechanism is shown in Fig. 9. The numerous electrons in the conduction band and the photogenerated holes in the valence band can activate the imidazole and phenylboronic acid in the MeOH solution to form the cross-coupling product.^{48–50}

The above results demonstrate that the optimized conditions were catalysis by Cu₂S:NiS₂@C/rGO using MeOH : H₂O (3 : 1) as the solvent at ambient temperature (25 °C) for 6 h under open-air conditions. The optimized Cu₂S:NiS₂@C/rGO-promoted photocatalytic C–N coupling of phenylboronic acid

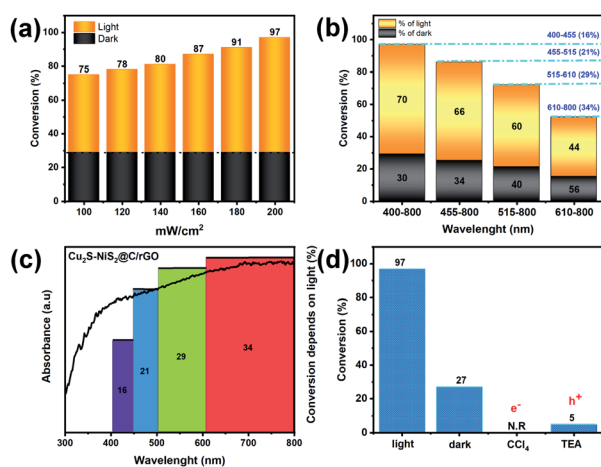


Fig. 8 (a) The dependence of (a) light intensity, (b) wavelength, (c) UV-Vis DRS absorption of Cu₂S:NiS₂@C/rGO and (d) electron–hole aspect photocatalyst.

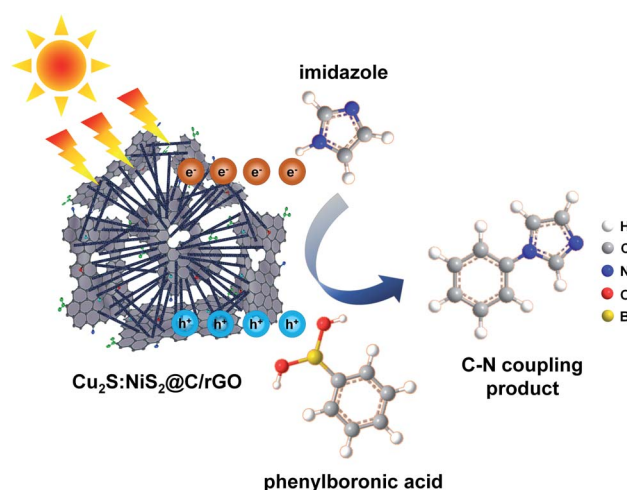


Fig. 9 Plausible mechanism for the visible light activated photocatalytic C–N coupling of phenylboronic acid and imidazole.

Table 2 The photocatalytic performance of Cu₂S:NiS₂@C/rGO for the C–N coupling of phenylboronic acid and imidazole with various moieties^a

Entry	1a	1b	Product	Conv. ^b (%)	Selec. ^b (%)
1				97	96
2				91	95
3				96	98
4				>99	98
5				95	97
6				97	98
7				97	96
8				>99	>99

^a Reaction conditions: 0.5 mmol of **1a** and **1b**, 4 mL solvent, 5 mg of photocatalyst. The reactions were conducted in air at r.t for 6 h, under Xe-lamp irradiation (400–800 nm) with a light intensity of 200 mW cm⁻². ^b Conversions (base on **1b**) and selectivity determined by GC-MS analysis.

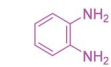
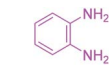
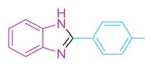
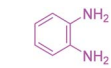
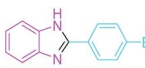
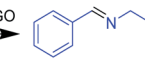
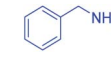
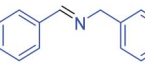
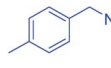
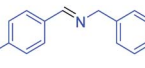
and imidazole was then applied to various substrates, as shown in Table 2. The explored diverse range of reactants with modified electron-donating groups did not significantly affect the reaction (entries 1–4). For electron-donating groups (entries 5–7), the conversion and selectivity remained >90%. Aromatic and heteroatomic boronic acids, such as N-containing heteroatomic boronic acids (entry 8), achieved high conversion and selectivity to the desired product. These phenomena led to a photocatalytic activity with remarkable functional group selectivity under mild conditions.

In addition to enhancing the catalytic performance, Cu₂S:NiS₂@C/rGO was used for the synthesis of other N-compound derivatives, such as N-heterocyclic and N-aryl derivatives. The N-heterocyclic product was obtained through the oxidative cyclization of *o*-phenylenediamine and aromatic aldehyde. The benzimidazole product was obtained by using 0.25 mmol of both substrates with EtOH as the solvent at room temperature for 1 h (Table 3, entries 1–3). Moreover, the presence of electron-donating and electron-withdrawing substituents resulted in excellent conversion and high selectivity. The oxidation of benzylamine to imines was selected as an example of generating N-aryl derivatives. Photo-activated Cu₂S:NiS₂@C/rGO synthesis

of imine was conducted for 4 h using 0.25 mmol of reactants and CH₃CN as the solvent (Table 3, entries 4–6). A satisfactory completed reaction and the synthesis of N-heterocyclic derivatives bearing electron-donating or electron-withdrawing moieties were achieved.

In addition to catalytic activity, reusability is also a key consideration in organic synthesis using heterogeneous catalysts. With the model reaction and optimized conditions in Table 1, the catalyst was reused for five cycles after being recovered through simple centrifugation and then washed with EtOH. The results in Fig. 10a demonstrate good recyclability with high conversion and selectivity values. Moreover, the stability of the Cu₂S:NiS₂@C/rGO catalyst was evaluated. The surface structures before and after usage were analyzed *via* XPS. The C 1s, Cu 2p, Ni 2p, and S 2p spectra of the photocatalyst before and after 5 cycles of usage were insignificantly different (Fig. 10b). The XRD-verified crystalline structure showed minimal changes in intensity without changing the main structure (Fig. S5a†). The morphology was characterized *via* TEM (Fig. S5b and c†), and results showed the tendency of the photocatalyst to preserve its form.

Table 3 The photocatalytic performance of $\text{Cu}_2\text{S}:\text{NiS}_2@\text{C}/\text{rGO}$ for the N-substituted derivatives with various moieties^a

Entry	1a	1b	Product	Conv. ^b (%)	Sele. ^b (%)
1				98	99
2				92	95
3				98	99
4				95	99
5				93	99
6				95	99

^a Reaction conditions: entry 1–3: 0.25 mmol of **1a** and **1b**, 3 mL EtOH, 2.5 mg of the photocatalyst, reactions for 1 h, conversions base on **1b**. Entry 4–6: 0.25 mmol reactant, 3 mL CH_3CN , 5 mg of the photocatalyst, reactions for 6 h. The reactions were conducted in air at r.t., under Xe-lamp irradiation (400–800 nm) with a light intensity of 200 mW cm^{-2} . ^b Conversions and selectivity determined by GC-MS analysis.

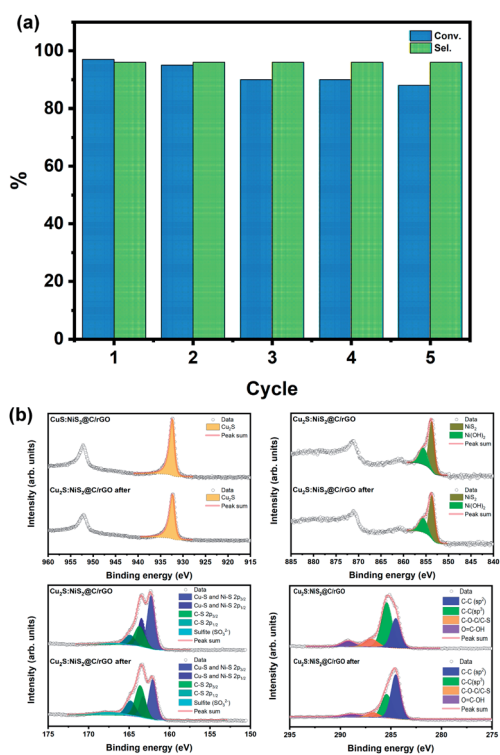


Fig. 10 (a) Reusability study for the photocatalytic activity of $\text{Cu}_2\text{S}:\text{NiS}_2@\text{C}/\text{rGO}$ and (b) XPS analysis of $\text{Cu}_2\text{S}:\text{NiS}_2@\text{C}/\text{rGO}$ photocatalyst after the reusability test.

Conclusions

A series of bimetallic MOFs using Cu and Ni as metal centers connected with a carboxylate-group-rich H_4BTEC ligand was synthesized through a facile and simple method. Subsequently, a hybrid core-shell nanostructure of bimetallic Cu and Ni sulfide encapsulated on porous C tailoring with GO was fabricated from an MOF derivative. Direct carbonization and sulfurization of the MOF ($\text{Cu}:\text{Ni-BTEC}/\text{GO}$) produced the bimetallic sulfide $\text{Cu}_2\text{S}:\text{NiS}_2@\text{C}/\text{rGO}$. $\text{Cu}_2\text{S}:\text{NiS}_2@\text{C}/\text{rGO}$ exhibited excellent photocatalytic properties and enhanced photocatalytic activity. The light-activated material $\text{Cu}_2\text{S}:\text{NiS}_2@\text{C}/\text{rGO}$ photogenerated holes and electrons, resulting in improved products of the C–N coupling of phenylboronic acid with imidazole, cyclization of *o*-phenylenediamine with aldehyde, and oxidative homocoupling reactions of benzylamine. The synergetic combination of non-noble metals Cu and Ni in the multifunctional structure of the bimetallic sulfide enhanced the photocatalytic activity of N-derivative compounds synthesized through oxidative coupling reactions. In addition, the recyclability and stability as important aspects of the heterogeneous catalyst were established. This hybrid structure can offer additional options for synthesizing core-shell structures through MOF derivation and lead to wide-ranging applications, such as in organic synthesis.

Conflicts of interest

There are no conflicts to declare.

Acknowledgements

This research was supported by Basic Science Research Program through the National Research Foundation of Korea (NRF) grant funded by the Korea Government (NRF-2020R1I1A3067208 and NRF-2018R1D1A1B07045663). S. Song was supported by the Global Ph.D. Fellowship Program (NRF-2018H1A2A1062253).

References

- H. Song, *Acc. Chem. Res.*, 2015, **48**, 491–499.
- A. M. El-Toni, M. A. Habila, J. P. Labis, Z. A. Allothman, M. Alhoshan, A. A. Elzatahry and F. Zhang, *Nanoscale*, 2016, **8**, 2510–2531.
- X. Yu, L. Wang and S. M. Cohen, *CrystEngComm*, 2017, **19**, 4126–4136.
- C. Sen Liu, J. Li and H. Pang, *Coord. Chem. Rev.*, 2020, **410**, 213222.
- M. H. Yap, K. L. Fow and G. Z. Chen, *Green Energy Environ.*, 2017, **2**, 218–245.
- Q. L. Zhu and Q. Xu, *Chem. Soc. Rev.*, 2014, **43**, 5468–5512.
- S. A. Hira, M. Nallal, K. Rajendran, S. Song, S. Park, J. M. Lee, S. H. Joo and K. H. Park, *Anal. Chim. Acta*, 2020, **1118**, 26–35.
- C. Gu, J. Li, J. P. Liu, H. Wang, Y. Peng and C. Sen Liu, *Appl. Catal., B*, 2021, **286**, 119888.
- D. Shi, R. Zheng, M. J. Sun, X. Cao, C. X. Sun, C. J. Cui, C. Sen Liu, J. Zhao and M. Du, *Angew. Chem., Int. Ed.*, 2017, **56**, 14637–14641.
- Y. Zheng, S. Zheng, H. Xue and H. Pang, *Adv. Funct. Mater.*, 2018, **28**.
- A. Han, B. Wang, A. Kumar, Y. Qin, J. Jin, X. Wang, C. Yang, B. Dong, Y. Jia, J. Liu and X. Sun, *Small Methods*, 2019, **3**, 1800471.
- J. Hwang, A. Ejsmont, R. Freund, J. Goscianska, B. V. K. J. Schmidt and S. Wuttke, *Chem. Soc. Rev.*, 2020, **49**, 3348–3422.
- F. Marpaung, M. Kim, J. H. Khan, K. Konstantinov, Y. Yamauchi, M. S. A. Hossain, J. Na and J. Kim, *Chem.–Asian J.*, 2019, **14**, 1331–1343.
- W. Zhan, L. Sun and X. Han, *Nano-Micro Lett.*, 2019, **11**, 1.
- L. Nie and Q. Zhang, *Inorg. Chem. Front.*, 2017, **4**, 1953–1962.
- S. Chandrasekaran, L. Yao, L. Deng, C. Bowen, Y. Zhang, S. Chen, Z. Lin, F. Peng and P. Zhang, *Chem. Soc. Rev.*, 2019, **48**, 4178–4280.
- M. Gao, L. Zhu, W. L. Ong, J. Wang and G. W. Ho, *Catal. Sci. Technol.*, 2015, **5**, 4703–4726.
- M. B. Gawande, A. Goswami, T. Asefa, H. Guo, A. V. Biradar, D. L. Peng, R. Zboril and R. S. Varma, *Chem. Soc. Rev.*, 2015, **44**, 7540–7590.
- H. Kweon, S. Jang, A. Bereketova, J. Chan Park and K. H. Park, *RSC Adv.*, 2019, **9**, 14154–14159.
- S. Ju, M. Yusuf, S. Jang, H. Kang, S. Kim and K. H. Park, *Chem.–Eur. J.*, 2019, **25**, 7852–7859.
- D. Kim, H. Kang, H. Park, S. Park, J. C. Park and K. H. Park, *Eur. J. Inorg. Chem.*, 2016, **2016**, 3469–3473.
- A. Kim, N. Muthuchamy, C. Yoon, S. Joo and K. Park, *Nanomaterials*, 2018, **8**, 138.
- S. Kim, S. W. Kang, A. Kim, M. Yusuf, J. C. Park and K. H. Park, *RSC Adv.*, 2018, **8**, 6200–6205.
- M. Yusuf, S. Song, S. Park and K. H. Park, *Appl. Catal., A*, 2021, **613**, 118025.
- X. Lang, X. Chen and J. Zhao, *Chem. Soc. Rev.*, 2014, **43**, 473–486.
- B. König, *Eur. J. Org. Chem.*, 2017, **2017**, 1979–1981.
- C. Fischer and B. Koenig, *Beilstein J. Org. Chem.*, 2011, **7**, 59–74.
- Salahuddin, M. Shaharyar and A. Mazumder, *Arabian J. Chem.*, 2017, **10**, S157–S173.
- N. Kerru, L. Gummidi, S. Maddila, K. K. Gangu and S. B. Jonnalagadda, *Molecules*, 2020, **25**, 1909.
- Y. Wang, W. X. Zhang and Z. Xi, *Chem. Soc. Rev.*, 2020, **49**, 5810–5849.
- Y. Bansal and O. Silakari, *Bioorg. Med. Chem.*, 2012, **20**, 6208–6236.
- C. M. Da Silva, D. L. Da Silva, L. V. Modolo, R. B. Alves, M. A. De Resende, C. V. B. Martins and Á. De Fátima, *J. Adv. Res.*, 2011, **2**, 1–8.
- J. Chen, J. Li and Z. Dong, *Adv. Synth. Catal.*, 2020, **362**, 3311–3331.
- G. Yan, Y. Zhang and J. Wang, *Adv. Synth. Catal.*, 2017, **359**, 4068–4105.
- Nitrogen Compounds, *Enological Chemistry*, ed. J. Moreno and R. Peinado, Elsevier, 2012, pp. 183–193.
- F. Su, S. C. Mathew, L. Möhlmann, M. Antonietti, X. Wang and S. Blechert, *Angew. Chem., Int. Ed.*, 2011, **50**, 657–660.
- V. N. Mahire and P. P. Mahulikar, *Chin. Chem. Lett.*, 2015, **26**, 983–987.
- R. Seetharaj, P. V. Vandana, P. Arya and S. Mathew, *Arabian J. Chem.*, 2019, **12**, 295–315.
- M. Q. Yang and Y. J. Xu, *Phys. Chem. Chem. Phys.*, 2013, **15**, 19102–19118.
- K. Dave, K. H. Park and M. Dhayal, *RSC Adv.*, 2015, **5**, 95657–95665.
- A. K. Das, M. Srivastav, R. K. Layek, M. E. Uddin, D. Jung, N. H. Kim and J. H. Lee, *J. Mater. Chem. A*, 2014, **2**, 1332–1340.
- Z. A. Allothman, *Materials*, 2012, **5**, 2874–2902.
- S. Ando, Y. Hirota, H. Matsunaga and T. Ishizuka, *Tetrahedron Lett.*, 2019, **60**, 1277–1280.
- K. A. S. Usman, J. W. Maina, S. Seyedin, M. T. Conato, L. M. Payawan, L. F. Dumée and J. M. Razal, *NPG Asia Mater.*, 2020, **12**(1), DOI: 10.1038/s41427-020-00240-5.
- X. Cai, Z. Xie, D. Li, M. Kassymova, S. Q. Zang and H. L. Jiang, *Coord. Chem. Rev.*, 2020, **417**, 213366.
- C. Capello, U. Fischer and K. Hungerbühler, *Green Chem.*, 2007, **9**, 927–993.
- J. Xiong, Q. Sun, J. Chen, Z. Li and S. Dou, *CrystEngComm*, 2016, **18**, 1713–1722.
- T. Garnier, R. Sakly, M. Danel, S. Chassaing and P. Pale, *Synth.*, 2017, **49**, 1223–1230.
- S. Rohani, A. Ziarati, G. M. Ziarani, A. Badiei and T. Burgi, *Catal. Sci. Technol.*, 2019, **9**, 3820–3827.
- J. Chen, J. Li and Z. Dong, *Adv. Synth. Catal.*, 2020, **362**, 3311–3331.